Faculty Publications, Chemistry   Chemistry

1-1-2002

Chemical analysis by X-ray spectroscopy near phase transitions in the solid state

Juana Vivó Acrivos
San Jose State University, juana.acrivos@sjsu.edu

L. Nguyen
San José State University

T. Norman
San José State University

C. T. Lin
IRC for Superconductivity, Cavendish Laboratory, Cambridge CB3 OHE UK

W. Y. Liang
IRC for Superconductivity, Cavendish Laboratory, Cambridge CB3 OHE UK

See next page for additional authors

Recommended Citation

Authors

Juana Vivó Acrivos, L. Nguyen, T. Norman, C. T. Lin, W. Y. Liang, J. M. Honig, and P Somasundaran

Chemical analysis by X-Ray spectroscopy near phase transitions in the solid state

Juana Vivó Acrivos*, L. Nguyen and T. Norman

San José State University, San José CA95192-0101

C.T. Lin and W.Y. Liang

IRC for Superconductivity, Cavendish Laboratory, Cambridge CB3 OHE UK

J.M. Honig, P. Somasundaran

Purdue University, Lafayette IN 47907-1393

2

Abstract

        The methods discussed in this work show that the types of changes which may be observed, by precise XAS measurements of Absorbance A versus temperature, across a phase transition are: the changes in the relaxation time of the final states t due to fluctuations near a phase transition; the detection of the anomalous Bragg condition coupled to phonon modes XAS enhancement that identifies the temperature interval where the phonon modes are active, the symmetry changes which introduce new allowed transitions to finite states below an element edge, near T_c indicate what symmetry changes occur, and the method of $XTDAFS_{T0} = XAFS(T) - XAFS(T_0)$, allows the precise measurement of the progressive changes in the Debye-Waller factor versus T near a phase transition, and identify (when no other structural changes occur, except in the vibrational modes of a specific bond) the bond responsible for the transition. The methods have been applied to the superconducting transition in layer cuprates and the metal to insulator transition in $NiS_{2-x}Se_x$.

_____

* Telephone: 1 408 924 4972; fax: 1 408 924 4945

* email: jacrivos@athens.sjsu.edu

3

-

Outline

1. Introduction to chemical analysis of Solids by X-Ray absorption spectroscopy

2. Experimental:

   2.1 Instrumentation details for XAS

       2.1.1   Optical density measurements

       2.1.2   Calibration procedures

   2.2 Applications to solid state phase transitions

       2.2.1   Materials

       2.2.2   Temperature control

       2.2.3   Precision

3. Discussion

   3.1 Electromagnetic relations

   3.2 Phase transitions

   3.3 Phenomena observed at phase transitions

4. Conclusions

   4.1 Use of techniques

   4.2 Phenomena

5. Acknowledgements

6. References

7. List of figures

8. Figures

1. Introduction

Continued innovation in synchrotron radiation facilities (up to 3rd generation at present) have provided improvements that allow new types of measurements in the study of solid state phase transitions using X-ray absorption spectroscopy (XAS) that were not possible up to date. This review article addresses the feasibility of accurate measurements that determine what changes occur in the valence, the bond order and the structure of materials undergoing phase transitions. This type of chemical analysis is important for the design of new materials with desired properties for applications in the solid state industry. This work describes the instrumental calibration, and stability required for accurate measurements, and the supporting theory that can give information on new phenomena. Examples of the different phenomena observed in different types of phase transitions will show the power of the method.

The phase transitions in solids are driven by a large variety of electronic processes that in turn lead to structural changes. A material may exhibit different phases, e.g. [1],

Metal / Insulator / Superconductor / Antiferromagnetic / Ferromagnetic / etc., (1)

according to the ambient temperature T, pressure P, and free electron concentration.

2. Experimental

2.1 Instrumentation details

All syncrotron facilities supply photons with varying degrees of monochromaticity. Figure 1 gives the diagram of a spectrometer used at the Stanford Synchrotron Radiation Laboratory (ssrl) for the work reported here.

2.1.1 Optical density measurements

The optical density is determined from the current I_i measured at different ionization chambers that constitute the spectrometer in Figure 1, where the sub index i identifies what the ionization chamber measures: 0, the incident radiation; 1, the radiation transmitted by the sample; and 2, the radiation transmitted by the reference material. The textbook [2] definition of Absorbance at given frequency v:

$$A_v = -Log_{10}T_{rv} \tag{2}$$

is determined from the Transmittance of the sample $T_{rv} = I_{1v}/I_{0v}$ at the frequency v. The X-ray energies hv are determined by the angle Θ that white synchrotron radiation makes with the diffraction planes (hkl) of two parallel Si crystals in the monochromator. The possibility of higher harmonics, nhv is always present because of allowed diffractions n(hkl). The higher harmonics can be eliminated because their rocking curves are sharper than for the fundamental, but these must be eliminated by calibration procedures in every experiment in order to eliminate uncertainties.

2.1.2 Calibration procedures

The frequency is selected by diffraction, and a fraction x of higher harmonics nv ($n \geq 2$) present in the beam must be ascertained. If I_0 and I_1 are the currents measured at

the respective ionization chambers, and x is the fraction of higher harmonics in the

incident beam and x' is that in the transmitted beam then:

$$I_{0,v} = (1 - x) I_0, \quad \Sigma_{n \neq 1} I_{0,nv} = x I_0,$$

$$I_{1,v} = (1 - x') I_1, \quad \Sigma_{n \neq 1} I_{1,nv} = x' I_1,$$

$$x' /(1 - x') = x 10^{A_v} /(1 - x). \tag{3}$$

The measured Absorbance $A = Log_{10}(I_0/I_1)$ approaches A_v only as x approaches zero, i.e.,

$$A_v - A = Log_{10}((1 - x)/(1 - x')) = Log_{10}(1 + x (10^{A_v} - 1))$$

$$\rightarrow x (10^{A_v} - 1) /Ln(10) \geq 0, \text{ as } x \rightarrow 0. \tag{4}$$

Since a monochromatic beam is essential for accurate measurements, it is achieved by

detuning the second Si crystal in the monochromator from the exact diffraction angle by

$\Delta\Theta$ with a piezoelectric device (Figure 1). Negligible harmonic content is usually

obtained by an 80% detuning of I_0 [3]. The higher harmonics nv are eliminated because

they are narrower than the fundamental diffraction, which is then shifted by the amount

$\Delta E = E \cot\Theta \Delta\Theta$ [4a]. Attention to these calibration details must be done to achieve the

desired accuracy. The monochromaticity of the beam is determined in the limit of $A_v/A =$

1 (Figure 2a,b). At 80% detuning, $x \rightarrow 0$, and a 4 eV shift is observed at the Cu_K edge

with a (111) Si cut crystal. The reason for this is that the detuning shifts the energy to

where the sharper higher harmonic [Figure 5 of ref. 4] practically disappears, but the

principal harmonic still has 20% intensity. By measuring the intensities of the

fundamental and the higher harmonics, Latimer et al. [3] have confirmed that 80 %

detuning indeed produces a monochromatic beam of very high v monochromaticity.

Throughout an experiment the stability of A_{v2} and E_{02} for the reference compound

(measured by I_2 in the spectrometer shown in Figure 1) is used to determine the limits of

accuracy. The rejection of the higher harmonics depends on the edge being measured and must be done for every experiment. The raw data for the sample versus temperature T can only be analyzed after the reference (kept at room temperature) shows the desired stability obtained with an I_0 detuning of 80% (Figure 2c). Fluorescence measurements can not be checked for accuracy with I_2.

The temperature is monitored with an Oxford 9000 cryogenic system and recorded digitally with Oxford Object Bench PC software. Typical measurements are carried out in complete temperature cycles (insert, Figure 2c).

2.2 Applications to solid state phase transitions

2.2.1   Materials

The methods have been applied to materials that are metals and insulators, cubic materials and low dimensional solids (LDS). These vary from superconductors, antiferromagnetic and ferromagnetic insulating and conducting materials: $YBa_2Cu_3O_{7-\delta}$ single crystal prepared at IRC for Superconductivity [5], $Nd(Ba_{0.95}Nd_{0.05})_2Cu_3O_7$ powders prepared at Morris Laboratories [6] and $NiS_{2-x}Se_x$ prepared at Purdue University [7]. A typical sample mount that goes inside the cryostat (Figure 1) is shown in Figure 3, together with the $YBa_2Cu_3O_{7-\delta}$ single crystal orientation used in this work.

2.2.2   Temperature Control

The data is acquired in temperature cycles. The reproducibility of the reference spectra in a given temperature cycle is very important. Reproducibility must be verified (Figure 2c) [8].

2.2.3 Precision

Once the data is obtained to a given precision, the analysis is carried out by measuring the following parameters: the X-ray absorption for excitations to bound states near an element edge, XANES; the edge energies, E_0; the X-ray absorption fine structure, XAFS and the X-ray temperature difference absorption spectra XTDAS [9]:

$$XTDAS_{T_0} = A_\nu(T) - A_\nu(T_0), \qquad (5)$$

is used to ascertain the changes in XAS relative to a temperature T_0 which may be near or above the phase transition temperature. New phenomena are determined as follows:

2.2.3.1 Changes in bond distance are determined by XAFS analysis [10].

2.2.3.2 Changes in bond order are determined by the so called atomic XAFS, (AT)AXAFS [11]. Here the X-ray fine structure changes due to a variation of the bond order. Electron density changes at distances less than an Ångstrom from the heavy absorbing heavy atom [11] are observed near the phase transition by XTDAS [12].

2.2.3.3 Changes in oxidation states are determined by precise measurements of edge shifts, to the accuracy given by the reference edge measurements [4].

2.2.3.4 Changes in the XANES may also occur if there are changes in the symmetry and the density of final states $N(E_E)$ near a phase transition [9,10,12].

3. Discussion

3.1 Electromagnetic radiation relations for XAS

A basic knowledge of the electromagnetic theory [2] involved in XAS is necessary for the interpretation of data. The excitation of electrons in core states to states

in a continuum of high kinetic energy probe the local potential for the absorber A. The

angular dependence of the X-ray absorption cross section $\sigma(\omega)$ [13] for a particle at $\mathbf{r}$, of

mass m_e, charge q, and spin s gyromagnetic ratio g, moving in a static potential $V(\mathbf{r})$ and

under the influence of the electromagnetic radiation fields (Φ, $\mathbf{A}$) at a frequency $\omega = 2v\pi$,

crossing the unit area, normal to the propagation direction, at the rate $I(\omega) = 2\varepsilon_0 c|\mathbf{A}_0|^2 \omega^2$

is obtained from the Hamiltonian:

$$\mathbf{H} = \mathbf{H}_0 + [i\,q\,h/2\pi m_e\,\mathbf{A}\cdot\nabla + \boldsymbol{hc}] + q^2/2m_e\,\mathbf{A}^2 + q\,\Phi - (g\,q/2m_e)\,\mathbf{s}\cdot\mathbf{B}, \qquad (6)$$

where

$$\mathbf{H}_0 = -\,(h/2\pi)^2\,\nabla^2 + V(\mathbf{r}), \quad \mathbf{A}(\mathbf{r}, t), = \mathbf{A}_0\,\hat{\mathbf{e}}\,e^{i\,(\mathbf{k}\cdot\mathbf{r} - \omega t)} + hc,$$

hc is the Hermitiean conjugate, ε_0 is the permittivity of vacuum, c is the velocity of light,

$\hat{\mathbf{e}}$ is the unit polarization vector, $\mathbf{k}$ is the x-ray wave vector, and $2^{1/2}\mathbf{A}_0$ is the vector

potential amplitude. A perturbation W:

$$W(t) = W\,e^{-i\omega t} + hc,$$

gives a transition probability w per unit time:

$$w = 4\pi^2/h\,\Sigma_f\,|{<}f|W|i{>}|^2\,\delta(E_f - E_i - h\,v).$$

 If the perturbation consists of a plane wave satisfying the relation for the magnetic

induction $\mathbf{B} = \nabla \mathbf{x}\,\mathbf{A}$, the transition probability simplifies to:

$$w = (4\pi^2 q^2/hm_e^2)|\mathbf{A}_0|^2\,\Sigma_f\,|{<}f|\,e^{i\,(\mathbf{k}\cdot\mathbf{r} - \omega t)}\{\hat{\mathbf{e}}\cdot\nabla\,h/2\pi - (g/2)\,\mathbf{s}\,(\square\mathbf{k}\,\mathbf{x}\,\hat{\mathbf{e}})\}|i{>}|^2\,\delta(E_f - E_i - hv),$$

and, the absorption cross section defined as:

$$\sigma(\omega) = (w\,hv)/I(\omega)$$

is written, in the absence of magnetic interactions [13] in a series expansion:

$$\sigma(\omega) = 2\ \pi\ \alpha\ h\ \omega\ \Sigma g_{i,f}\ \{|<f|\mathbf{\hat{e}.r}|i>|^2 + 0.25\ |<f|\ \mathbf{\hat{e}.r\ k.r}|i>|^2+..\}\ \delta(E_f - E_i - h\nu).$$

(6.1)The important spectroscopic applications are derived from relation (6.1). The first and second terms in the expansion may be detected with highly polarized synchrotron radiation, giving rise to the dipolar and quadrupolar terms. Thus, one may detect any symmetry changes near a phase transition. The absorption cross section has several contributions:

3.1.1 The atomic (AT)XAS cross section K_A versus energy, $E = h\nu$ in the neighborhood of an X-ray edge ($E_0 = h\nu_0$) for the absorber A, is given by the sum of Lorentzian curves [14].

$$K_A(\tau,(\nu\text{-}\nu_0)) = \Sigma_{AE}\ a_A/[1+ (2\pi\ \tau)^2(\nu_{AE} - \nu)^2]$$

$$\rightarrow \int_0^{E\text{-}E0} N(E_E)/[1 + (m\ x)^2] = C_A\ \{\pi/2\ + atan(2\pi\ \tau\ (\nu - \nu_0)\},\qquad (6.2)$$

where a_A and C_A are constants determined by the material and $h\nu_{AE}$ is the excitation energy (Figure 4), the photoelectron wave vector is

$$k(\text{Å}^{-1}) = (0.2625(E - E_0))^{1/2}$$

when E is in eV, the initial and final states energies are E_A and E_E respectively,

$$\tau = 6.5821*10^{-16}\ s/HWHH,$$

$$E_{AE} = E_E - E_A = h\nu_{AE},$$

$$x = E - E_{AE},$$

$$m = 2\ \pi\ \tau/h,$$

HWHH is the half line width at half height in eV, and the final density of states $N(E_E)$ is determined by the states in the material.

The local potential $V(\mathbf{r})$ determines the states' lifetime. In the absence of fluctuations:

$$1/\tau = 1/\tau_{if} = (1/\tau_{\text{initial states}} + 1/\tau_{\text{final states}})/2. \tag{6.3}$$

For energies below an edge (near 5 to 13 keV) the natural relaxation times are determined from the magnitude of the half line widths (0.5 to 1 eV) to be $\tau_{if} \geq 10^{-16}$ s.

3.1.2 The analysis of multiple the transitions which occur immediately above the edge is complicated, but 50 eV above the edge the X-ray absorption fine structure (XAFS) modulates K_A, and is manipulated for structure analysis [9, 10, 14f] which is not included in this work: The photoelectron emitted by A travels to a neighboring atom B at a bond distance $R_{AB} \sim 3$ Å and back in less than 10^{-17} s. In the absence of fluctuations the measured relaxation time is $\tau = \tau_{if}$. In the presence of fluctuations in the potential, which limits the lifetime of the final state, the line width obtains:

$$1/\tau = 1/\tau_{if} + 1/\tau_{\text{fluctuations}}. \tag{6.4}$$

Thus, XAS is ideally suited to measure changes in the relaxation times of the order 10^{-16} to 10^{-17} s near a phase transition.

3.1.3 At room temperature, the transitions to states below the edge, XANES obey the symmetry selection rules, and the line widths give the natural lifetime of the final states of 10^{-16} s[11]. Any decrease in τ below 10^{-16} s can be detected by its effect on the atomic absorption coefficient K_A. Then the calculated absorption coefficient for atomic (AT)XAS, $K_A(m, E - E_0)$ and its variance versus $m = 2\pi\tau/h$, and $E - E_0$ (Figure 4a-d), are used to ascertain the value τ from the data (Figure 5a), i.e.,

$$m(T)/m(T_c) = \tau(T)/\tau(T_c) =$$

$$(1/10^{-16} s + 1/\tau_{\text{fluctuations}}(T_c))/(1/10^{-16} s + 1/\tau_{\text{fluctuations}}(T))$$

$$\rightarrow \tau(T)/\tau_{\text{fluctuations}}(T_c). \tag{6.5}$$

Once the correct accuracy is achieved, the XAFS, XTDAS, (AT)XAS and (AT)XAFS are analyzed by computer programs developed during the last ten years in the literature [14]. Only then can the phenomena that occur near a phase transition can be accurately ascertained.

3.2 Phase Transitions

The phenomena which occur near two types of phase transitions will be described here with the purpose to show the power of the method.

3.2.1 Metal to Superconductor Phase Transitions

The metal to superconductor transition is studied in the layered cuprate materials, $YBa_2Cu_3O_{7-\delta}$ and $Nd(Ba_{0.95}Nd_{0.05})_2Cu_3O_7$ at the Cu_K, Y_K, Ba_L and Nd_L edges versus temperature T.

3.2.1.1 The Cu_K XANES provide an example to show how the changes in symmetry at the transition temperature can be detected. An as grown $YBa_2Cu_3O_{7-\delta}$ single crystal [5], labeled CT has a thickness $d_c \sim 22$ μm determined by Absorbance at the Cu_K, $Ba_{L3,2}$ and Y_K edges (Figures 5-7). The dipolar edge transitions, Cu 1s <-> n p_i are independent of the temperature (Figure 5) at the at a crystal orientation relative to the X-ray polarization direction ε_{x-rays}, $\theta = \varepsilon_{x-rays}$ ^**c** when c is the sample crystallographic axis (Figure 3). The transitions' symmetry, in a single crystal, are identified by the orientation dependence of the amplitude versus θ. The baseline corrected raw data (Figure 5a) is manipulated to obtain important information as follows:

μ_A is evaluated (Figure 5d) by normalizing the absorbance A to the zero XAFS amplitude curve, extrapolated to the edge E_0:

$$\mu_A = A/A_{XAFS,0}.$$

μ_{AE} evaluates the amplitude of the transitions to finite states by subtracting the transitions to the continuum, relation (6.2) from μ_A (Figure 5g):

$$\mu_{AE} = \mu_A - \{1/2 + \Sigma_i(x_i \, atan(m(E - E_{0i}))/\pi\}$$

where $m = 2 \pi \tau/h \sim 0.3/eV$ ($\tau = 2.2 *10^{-16}$ s) and the mole fractions are $x_i = 1/3, 2/3$ for Cu in the CuO chains and in the CuO_2 planes respectively. A good fit is obtained from T = 49 to 100 K (Figure 5h) when the data is fitted to:

$$E_{0i=chains}-E_{0i=planes} = 6 \text{ eV}$$

in relation (6.2) for the respective valence states. It has been shown for elements with multiple valence, V that the edge position changes at a rate of $dE_0/dV \approx 5$ to 6 eV [4b,14f], which obtains:

$$V(\text{Cu in chains}) - V(\text{Cu in planes}) \approx 1$$

over the entire temperature interval.

μ_{CuEn} is evaluated (Figure 5e) to confirm the dipolar nature of the transitions:

$$\mu_{CuEn} = \mu_{CuE}(\theta)/cos(\theta).$$

When it is independent of θ the final states are assigned to 1s <-> $np_{x,y}$ transitions. Although the sample geometry prevents obtaining data for $\theta < \pi/4$, the presence of a transition 1s <-> n p_z is identified from $(\mu_{Cu}(\pi/4) -\mu_{Cu}(\pi/2))/sin(\pi/4)$ (Figure 5f).

$XTDAS_{Tc}$ are evaluated to determine if new allowed transitions appear, as a result of changes in the symmetry and density of final states $N(E_E)$ of the material, near a phase transition temperature T_c (Figures 5b, c):

$$XTDAS_{Tc} = A(T_c) - A(T \neq T_c).$$

These are two orders of magnitude lower in amplitude, but much broader than the dipolar transitions. HWHH ~ 10 eV obtain τ ~ $6.6*10^{-17}$ s. They have been assigned to the quadrupolar terms in relation (6.1), assuming that nd states become available at T_c.

The decrease in the atomic (AT)XAS absorption coefficient, K_{Cu} for high photoelectron kinetic energy (Figures 5a) at $T_{c1} = 93.1$, and $T_{c2} = 60 \pm 2$ K is assigned to a line broadening due to fluctuations. If this is due to a decrease in the lifetimes of the final states, we obtain for the crystal CT the same value derived from the XANES quadrupolar transitions line widths (Figure 5b, c):

$$\tau\,(T_c) \leq 1/2\,\tau\,(T \neq T_c) \approx 10^{-17}\,\text{s}.$$

The new clues given by the analysis are an increase in the final density of nd states, and an increase in the fluctuations which give rise to broader line widths, only near T_c.

3.2.1.2. The Ba_L edge spectra also provide new insight into the phenomena occurring near phase transitions. At the $Ba_{L3,2}$ edges the edge transitions are:

$$2p_{3/2,1/2} <-> \text{nd}.$$
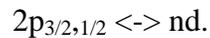
The XANES and XAFS (Figure 6a) are sharp (with less than 3 eV line widths) at all temperatures at the crystal orientation (Figure 3) $\theta = \pi/2$. Rotation from $\theta = \pi/2$ to $\theta = 8\pi/18$, produces a signal enhancement which increases as the temperature is lowered below 120 K (Figures 6b,c). The enhancement increases over two orders of magnitude (Figures 6d,e) as the temperature decreases below T_{c1}, and an interference pattern (Figure 6f) is observed with a period of 0.67 eV at the Ba_{L3} edge that increases at the Ba_{L2} edge 0.72 eV. These phenomena can be qualitatively explained by the propagation of electromagnetic radiation into the crystal by X-ray diffraction by individual planes

containing the Ba atoms coupled by a surface plasmon (when this appears at a given temperature T < 121 K) in a way which is similar to surface enhanced Raman scattering [16a]. Near λ = 2.36 Å (Ba_{L3} edge) and 2.20 Å (Ba_{L2} edge), at θ = 8π/18, there is an enhancement in the Ba planes' diffraction (which satisfy the Bragg condition S_{hkl} = 2 $\sin(\theta_{hkl})/\lambda$) due to absorption [15]. The diffracted wave length in the ith layer $\lambda_i = E_i/hc$ is determined by the index of refraction: $n_{i+1}/n_i = \lambda_i/\lambda_{i+1}$. The expression for n = 1- δ - $i\beta$ [15a] allows to estimate δ/layer ~ $7.7*10^{-6}$ for planes containing the Ba atom. If the interference period dE = 0.67 eV is produced by an energy and/or phase shift, on flux enhancement by diffraction, this must occur over 17 ~ layers or ~ 21 nm of sample is much smaller than the sample thickness d_c ~ 22 μm. This new phenomenom may be associated with the vibrational modes in the lattice that involve the Ba atoms [16]. Recent work [16a] shows that the Raman vibrational modes involving the Ba atoms and the O3A and O3B atoms (Figure 3) soften above 100 K in the related compound $YBa_2Cu_4O_8$. The phenomenom is not observed at Cu_K edge of CT near T_c [17] because there is no anomalous Bragg condition, nor at the Zn_K edge in $YBa_2Cu_{3-x}Zn_xO_{7-\delta}$ in the anomalous Bragg enhancement of diffraction at room temperature [16b], nor at other edges [16c] where the anomalous Bragg diffraction was measured only at room temperature. At least two conditions must be present to observe the enhancement, the coincidence of absorption with the Bragg condition and the presence of a plasmon [16a]. The Absorbance enhancement factor (Figure 6e):

$$\varepsilon_A = A(T)/A(T_{ref}) = \varepsilon_{K,Ba} \{1 + XAFS(T)/K_{Ba}(T)\}/\{1 + XAFS(T_{ref})/K_{Ba}(T_{ref})\}$$

$$-> \varepsilon_K \{1 + \Delta_{XAFS}\}$$

has contributions from the atomic absorption coefficient, $\varepsilon_{K,BaL3} = K_{BaL3}(T)/ K_{BaL3}(T_{ref})$

and since $XAFS(T) << K_{Ba,L3}(T)$ then $\Delta_{XAFS} \cong XAFS(T)/K(T) - XAFS(T_{ref})/K(T_{ref}) << 1$.

Thus the enhancement is mainly in $K_{Ba,L3}(T)$ as $T < T_c$, going through maxima versus E

when the anomalous Bragg condition is satisfied (Figure 6e) but the modulation follows

the XAFS signal [12]. The Raman studies of Watanabe et al. [16a] indicate that the Ba-

O3 and Ba-O2 modes soften below 130 K in $YBa_2Cu_4O_8$, so the modulation most

probably arise from corresponding changes in the XAFS.

The weighted k^3XTDAS for CT, at the Ba_{L3} edge (Figure 6h) between $T_1 <$

T_{c2}, and $T_2 > T_{c2} \sim 60 \pm 2$ K (Figure 5a) shows a long wave oscillation, which is not

present when both T_1, $T_2 > T_{c2}$ (insert Figure 6h). Complete oscillations are found for

the powder sample $Nd(Ba_{0.95}Nd_{0.05})_2Cu_3O_7$ (Figure 6i). These are attributed to atomic

(AT)XAFS observed at $(R_{electron\ density} + \Delta) < 1$ Å, in the Fourier Transform. These are

hard to interpret in condensed phases, because of the scattering from nearby atoms, and

features can only be measured in the XAS of gases [11], and in the Rb^+ vapor power

spectrum [11b]. If in a phase transition the only change that occurs is in the electron

density near a given site, it may be detected by (AT)XTDAFS for a heavy atom absorber

(e.g., Ba, Y). The long wave length oscillations observed versus the photoelectron wave

vector k (Figures 6i) with a period of $\Delta k \sim 4.5$ Å^{-1} (Figure 6i) do not correspond to a bond

change but to a change in electron density near the Ba atom near T_c for

$Nd(Ba_{0.95}Nd_{0.05})_2Cu_3O_7$. The advantage of XTDAS here is that the XAFS contributions

from all the other bonds were subtracted out, allowing one to identify the bonds and

electron density changes at the phase transition.

3.2.1.3 The orientation dependence at the Y_K edge confirms the dipolar nature of the edge transitions (Figure 7). Also weak interference fringes are observed at the same orientation as those observed near the Ba edge below T_{c1}. The Y_K edge occurs at $E_{0,Y_K} \sim 3\ E_{0,Ba^{L2}}$, and the anomalous Bragg condition would also satisfied for Y atoms in the Ba planes (Figure 7b), and the effect is reduced by the fraction of Y impurities. The Y_K edge XTDAFS (Figure 7 c-e) identify electron density changes near the Y atom, versus orientation, below T_{c1}. A decrease (negative XTDAFS) in electron density is observed when the polarization $\varepsilon_{X\text{-rays}}$ is in the crystal ab plane (Figure 7c) while it increases (positive XTDAFS) when the polarization is above the ab plane (Figures 7b,c).

3.2.2 Paramagnetic Metal to Antiferromagnetic Metal Phase Transitions

Paramagnetic to antiferromagnetic metal transitions by XAS are investigated for $NiS_{2-x}Se_x$ at the Ni_K and Se_K edges versus temperature and composition x. The base line corrected XAS (Figure 8a) show a different versus temperature dependence than for the metal to superconducting phase transition. The $XTDAFS_{7K} = A(7\ K) - A(T)$, for x = 0.47 (Figure 8b) [9b, 10b] are different than for x = 0.6 (Figure 8d-f) [8] which can be explained by the material phase diagram [1b] obtained from conductivity and magnetic susceptibility data (Figure 8c). From x = 0.4 to 0.5 there is a broad transition in the limit of 0 K from an antiferromagnetic (AF) insulator (I) to an AF metal (M) and the limit shifts to higher values of x-> 0.6 as the temperature in increased. The fraction of Se sites occupied at the onset of the transition, 20% is at the percolation limit for metallic conduction by the Se atoms in the cubic lattice. The new observations are:

3.2.2.1 The sharp Se_K edge $XTDAFS_{7K}$ oscillations observed for $NiS_{2-x}Se_x$ (Figure 8b, x = 0.47) correspond to the Se-Ni bond, $R_{Se-Ni} = 2.3$ Å. The advantage of XTDAFS in

the study of phase transitions in complicated structures is that only the bond responsible for the transition is selected.

3.2.2.2 When the phase diagram [1b] indicates that an electronic phase transition (Figure 8d) occurs near 36 K, the bond distance R_{S-Se} increases from 3.14 to 3.3 Å near 36 K (Figure 8c), as determined by XAFS analysis [10b]. If there are no structure changes other than an increase in the Debye-Waller factor for the Ni-Se bond with temperature (7-37 K), the $XTDAFS_{7K}$ oscillations represent the change between 7 to 27 K in the bond vibrations (Figure 8c).

3.2.2.3 At temperatures T > 37 K the structure changes, and XAFS(T) are not in phase with the XAFS(7 K) so the XTDAFS cancel by interference.

3.2.2.4 For x= 0.6 [8] the $XTDAFS_{7K-T}$ are similar to those for x = 0.47, which identifies that the Ni-Se bond is undergoing changes in the Debye-Waller factor as the temperature increases, in the metallic phase (Figure 8d) where the change in slope indicates there is a change in the lifetime of the final states. $\tau_{6K} > \tau_{7K} > \tau_{12K} > \tau_{20K} > \tau_{37K} > \tau_{51K} > \tau_{75K}$. The $XTDAFS_{7K}$ structure is still observable near 75 K. The phase diagram for x = 0.6 (Figure 8d) does indeed show that the metallic state still obtains at 75 K [1b].

For x= 0.6 [8], the $XTDAFS_{5-75K}$ (Figure 8g) indicate a change in the (AT)XAFS due to a decrease in electron density near the Se atom at 75 K relative to 7 K.

4. **Conclusions:**

4.1 The methods discussed in this work indicate what types of changes may be observed, by the XAS technique of precise measurements of Absorbance A versus temperature, across a phase transition. These are:

4.1.1   the changes in the relaxation time of the final states, $\tau_{final\ states}$ due to fluctuations near a phase transition,

4.1.2   the anomalous Bragg condition coupled to phonon modes   XAS enhancement identifies the temperature interval where the phonon modes are active,

4.1.3   the symmetry changes which introduce new allowed transitions to finite states below an element edge, near T_c indicate changes of symmetry,

4.1.4   the techniques of $XTDAS_{T1-T2}$ and $XTDAFS_{T1-T2}$, allows the detection of new transitions, and also precise measurement of the progressive changes in the Debye-Waller factor for a given bond, versus temperature when no other structural changes occur, except in the vibrational modes of a specific bond, which may in turn be responsible for the transition.

4.2   Also it is of some importance to determine the degree of thermodynamic stability [18] for the phenomena observed at a given phase transition as follows:

4.2.1   The interplay of charge transfer with the formation of charge density waves (CDW) and/or spin density waves (SDW) leads to fluctuations, that determines whether a superconducting or an antiferromagnetic state is formed at the metal to non-metal transition [19]. Understanding these effects can lead to the discovery of useful materials. The Boltzmann probability ($e^{S/kB}$) of a thermodynamic state is determined by its entropy S in units of the Boltzmann constant k_B. The system can be treated thermodynamically as long as its relaxation time τ is sufficiently long to produce small fluctuations, i.e., when $\Delta S/k_B \ll 1$ at a given temperature T [12, 18]. The Uncertainty Principle:

$$\Delta E\ \Delta S \sim T\ \ \Delta S\ \tau \geq h\ /4p, \tag{7}$$

20

where ΔE and ΔS are the uncertainty in energy and entropy, and h is Planck's obtains:

$$\Delta S/k_B \geq h/(4\pi \tau k_B T) \sim 3.82 *10^{-12}/\{\tau(s)\ T(K)\}. \tag{7.1}$$

Then, as long as $\tau T \geq 4$ ps K, the uncertainty $\Delta S/k_B$ is small compared to unity, and the system can be treated thermodynamically. Here relation (7.1) is applied to both antiferromagnetic and superconducting systems [1,12] in order to understand how the displacement in equilibrium to metals, insulators, and antiferromagnets and superconductors works.

4.2.2 Relation (7.1) obtains for cuprates $\Delta S(T_c)/k_B \gg 1$ indicating that fluctuations [12,19] are responsible for the transition to superconductivity. The superconducting transition in both single crystal and powder superconducting cuprates is associated with a change in the Ba electron density near T_c that is preceded by a Ba-O3A/B bond vibration softening where fluctuations can be studied.

4.2.3 The XTDAFS$_{7K-T}$ indicate that the Ni-Se bond is involved in the antiferromagnetic/ferromagnetic phase transitions in the Honig--Spałek phase diagram [1b] near 7 K in NiS$_{2-x}$Se$_x$ for x = 0.47 and 0.6. An increased domain order may be reflected in the longer relaxation time τ obtained below 7K in relation (7.1) (Figure 8a).

4.2.4 The XTDAFS$_{75K-7K}$ differentiate between x= 0.47 and 0.6 in the paramagnetic-insulating to paramagnetic/antiferromagnetic-metal transition for NiS$_{2-x}$Se$_x$.

5. Acknowledgments:

6. References:

1. (a) N. F. Mott, "*Metal to Insulator Transition*", Taylor and Francis, 1974, 1990; (b) J.M. Honig and J. Spałek, *Chem. Mater*, **10**, 2810 (1998)

2. P.W. Atkins, "*Physical Chemistry*", 6th Edition , W.H. Freeman and Co, New York, 1998

3. M. J. Latimer, A. Rompel, J. H. Underwood, V.K. Yachandra and M.P. Klein, *Rev. Sci. Instrum.* **66,** 1843 (1995)

4. J.V. Acrivos, K. Hathaway, J. Reynolds, J. Code, S. Parkin, M.P. Klein, A. Thompson and D. Goodin, *Rev. Sci. Instrum.* **53**, 575 (1982);

5. C.T. Lin, W.Zhou and Y. W. Liang, *Physica C*, 195 291 (1992)

6. J.V. Acrivos, Lei Chen, P. Metcalf, J.M. Honig, R.S. Liu and K.K. Singh, *Phys. Rev. B*, **50**, 13710 (1994)

7. X. Yao and J.M. Honig, *Mater. Res. Bull.* **29**, 709 (1994)

8. J.V. Acrivos and R. Shaikh, unpublished (2000)

9. (a) L. Nguyen, et al., Am. Phy. Soc. March Meeting, *Bull Am Phys. Soc.,***43**, 345 (1998); (b) T. Norman et al., Am. Phy. Soc. March Meeting, *Bull Am Phys. Soc.,* **43**, 871 (1998); (c) T. Norman, L. Nguyen, A. T. Nguyen, C. M. Burch, T. H. Vu, Q. van Le, J. V. Acrivos, "*Stanford Synchrotron Radiation Laboratory Activity Report*" 2375M, (1997);

10. (a) L. Nguyen, "*MS Thesis*", SJSU (2000); (b) T. Norman, "*M.S. Thesis*", SJSU (2000); (c) J.V. Acrivos, Lei Chen and C.M. Burch, *Superlattices and Microstructures*, **18,** 197 (1995)

11. (a) A.L. Ankudinov and J.J. Rehr, *J. Phys. IV France 7*, **C2**- 121 (1997); (b) A. Kodre, I. Arçon and R. Frahm, *ibid*., **C2**-195 (1997); (c) Y.A. Babanov, A.V. Ryazhkin and A.F. Sidorenko, *ibid*, **C2**-277 (1997)

12. J.V. Acrivos, *Solid State Sciences,* **2**, 807 (2000)

13. C. Brouder, *J. Phys.:Condens. Matter* **2**, 701 (1990)

14. (a) F.K. Richtmyer, S.W. Barnes and E. Ramberg, *Phys. Rev.* **46**, 843 (1934); (b) A. Kodre, I. Arçon and R. Frahm, *Physica*, **C2**-195 (1997); (c) Y.A. Babanov, A.V. Ryazhkin and A.F. Sidorenko, *ibid*, **C2**-277 (1997); (d) G. Li, F. Bridges, G.S. Brown, Phys. Rev. Lett 68, 1609 (1992); (e) D.H. Templeton, *Handbook of Synchrotron Radiation*, **3**, 201 (1991), eds., G. Brown and D.E. Moncton, Elsevier; (f) B.K. Teo, "*EXAFS"*, Springer-Verlag, Berlin (1985)

15. (a) D.H. Templeton, *Handbook of Synchrotron Radiation*, **3**, 201 (1991), eds., G. Brown and D.E. Moncton, Elsevier; (b) R.S. Howland, T.H. Geballe, S.S. Laderman, A. Fischer-Colbrie, M. Scott, J.M. tarascon, P. Barboux, *Phys.Rev.,* **B39**, 9017 (1989); (c) M.A. Aranda, D.C. Sinclair, J.P. Attfield, A.P. MacKenzie, *Phys. Rev.,* **B51**, 12747 (1995)

16. (a) N. Watanabe and N. Koshizuka, *Advances in Superconductivity IX,* p. 153 , Springer-Verlag, Tokyo (1997); (b) C. Thomsen and M. Cardona, *Physical Properties of High Tc Superconductors I,* p. 409 (1988), World Scientific, D. M. Ginsberg, ed

17. C. H. Booth, F. Bridges, J.M Boyce, T. Claeson, B.M. Lairson, R. Liang, and D. Bonn, *Phys. Rev.,* **B54**, 9542 (1996)

18. (a) L.D. Landau and E.M. Lifshitz, "*Statistical Physics"*, translated by J.B. Sykes and M.J. Kearsley, Pergamon Press NY 1993; (b) P.G. de Gennes, *Phys Rev.* **118,** 141 (1960); (c) C. Castellani, C. Di Castro and M. Grilli, *Z. Phys. B* **103**, 137 (1997)

7. List of Figures:

Figure 1: XAS spectrometer configuration for the measurement in transmission at SSRL, station 2-3.

Figure 2: XAS spectrometer calibration as $A_v/A \rightarrow 1$. (**a**)100 A_v/A versus the actual counts measured in the real time clock **rtc/I$_0$** at the Cu$_K$ edge. (**b**) Shift in the value E$_0$ at the Cu$_K$ edge in a Cu metal thin film, as $A_v/A \rightarrow 1$. (c) **XAS** spectrometer temperature T measurement: the actual sample $NiS_{2-x}Se_x$ A versus T, compared with the constancy of the reference A for a Se film. The insert shows the actual temperature T cycle for the measurment.

Figure 3: Mounted crystal $YBa_2Cu_3O_{7-\delta}$. Photograph of a crystal (CT) mounted in the Al holder that goes into the cryostat (Figure 1). A lead mask, with a center hole (same shape as the crystal) covers it. A grid with $\pi/6$ angle marks is used to determines the azimuthal orientation ϕ. The angle that the crystal c-axis makes with the X-ray polarization vector: $\theta = \mathbf{c}^{\wedge}\mathbf{\varepsilon}_{X\text{-rays}}$ is determined outside the cryostat by a goniometer to $\pm$ 2 DEG.

Figure 4: Calculated atomic absorption coefficient: (a) K versus m and E- E$_0$. (b) K versus E$_F$ and E-E$_0$. (c) K(m = 1 eV^{-1}) versus E-E$_0$. (d) Variance of K versus m and E-E$_0$.

Figure 5: Cu$_K$ edge XAS of Single Crystal $YBa_2Cu_3O_{7-d}$ (labeled CT) as grown at the IRC for superconductivity, ref. 5. (**a**) XAS versus T. The constant sample density versus T is ascertained by $A_{v,max}= 1.8$ Ln(10) versus T. (**b**) $A_{Cu}(60 \text{ K}) - <A_{Cu}(T \neq T_c)>$. (**c**) $A_{Cu}(92$ K) $- <A_{Cu}(T \neq T_c)>$. (**d**) μ_{Cu} versus E with two inserts: (**e**) $\mu_{CuEn} = \mu_{CuE}(\theta)/\cos(\theta)$ versus E confirms dipolar nature of edge transitions, and (**f**) $p_0 = \{\mu_{CuE}(\pi/4) - \mu_{CuE}(0)\}/\sin(\pi/4)$

obtains contribution from 1s <-> np_z transition versus E. **(g)** μ_{CuE} versus E at different θ gives the dipolar transitions at the edge. (h) μ_{CuE} (experimenytal) (48 to 100 K) compared to the sum of Lorentzian curves calculated μ_{CuE} for $E_0Cu(chains) - E_0Cu(planes) = 6$ eV.

Figure 6: $Ba_{L3,2}$ edge XAS of $YBa_2Cu_3O_{7-\delta}$ single crystal labeled CT and 2μm powder $Nd(Ba_{0.95}Nd_{0.05})_2Cu_3O_7$, 1:5 weight ratio in BN. **(a,b,c)** CT Ba_{L3} edge intensity for $\theta = \pi/2$ to $8\pi/18$ as T decreases below T_c. **(d)** $XTDAS_{121K}$ at $\theta = 8$ $\pi/18$. The Ba_{L2} $XTDAS_{121K}$ are multiplied by 5. A maximum is achieved above T_{c2}. **(e)** $Ba_{L3,2}$ XAS enhancement $\mathcal{E}_{BaL3,2}$ versus T at $\theta = 8$ $\pi/18$ at different temperatures. A maximum is achieved above T_{c2}. **(f), (g)** $A_{Ba}(L3)$, $A_{Ba}(L2)$ enhancement showing interference pattern at $\theta = 8$ $\pi/18$. **(h)** $k^3XTDAS_{T1,T2}$ at two T intervals: $T_{c1} > T_1 > T_{c2} > T_2$ and $T_{c1} > T_1, T_2 > T_{c2}$ showing a change in (AT)XAFS occurs below T_{c2} in Figure 5a. **(i)** $XTDAS_{Tc2}$ for the spectra Ba_{L3} edge XAS averaged over all temperatures 115 to 7 K, for 2μm powder $Nd(Ba_{0.95}Nd_{0.05})_2Cu_3O_7$. This identifies the second transition at T_{c2} with a change in the electron density near the Ba atom.

 Figure 7: Y_K edge XAS in $YBa_2Cu_3O_{7-\delta}$ labeled CT,: **(a)** $\mu_{YE}(\theta)$ versus θ, with orientation dependence similar to μ_{CuE}. **(b)** $\mu_{YE}(\pi/4) - \mu_{YE}(\theta = n\pi)$ at 65 K. When $\theta = 17\pi/36$, the interference fine structure is $dE_Y = 1.27$ eV ~ 2 dE_{Ba}. Here $\lambda = \lambda_{Ba L2-edge}/3$ Å indicates that third order diffractions of those near the Ba edge may be responsible for the interference pattern. The absorbers involved, may be those occurring as impurities in the Ba layer. **(c), (d), (e)** Change in Y AT-XAFS vs T at different θ below $T_c = 92$ K.

Figure 7: XTdAS for 2 μm size powder $NiS_{2-x}Se_x$ (x = 0.47: m3 cubic lattice a = b = c=5.753(9) Å in ref. 1b) diluted in 1 to 5 parts per weight in BN near the Se_K edge. The

spectrometer stability is confirmed by the Se film reference XAS, and the constant sample density by the constant edge $A_v = 0.125$ Ln(10) versus temperature for all the spectra.

Figure 8: XAS from a 2 μm size powdered $NiS_{2-x}Se_x$ m3 cubic lattice a=b=c=5.7539 Å [10b]): (**a**) (x=0.47, diluted in 1 to 5 parts per weight in BN, near the Se-K edge at different temperatures T. (**b**) $XTDAFS_{7K}$ versus the inverse photoelectron wave vector (x = 0.47) [10c]. (**c**) Se-S bond distance obtained by XAFS analysis [10b] showing a distinct structural change near 37 K. (**d**) Phase diagram versus composition [1b]. (**e, f**) $XTDAFS_{7K}$ versus the inverse photoelectron wave vector (x = 0.6) [8]. (**g**) $XTDAFS_{5K-75F}$ show (AT)XAFS due to a decrease in the electron density near the Se atom at 75 K relative to 5 K. This was not observed for the x = 0.47 sample.